

Vibrational spectra of dissociatively adsorbed D₂O on Al-terminated α -Al₂O₃(0001) surfaces from *ab initio* molecular dynamics

Cite as: J. Chem. Phys. **150**, 244701 (2019); <https://doi.org/10.1063/1.5099895>

Submitted: 12 April 2019 . Accepted: 23 May 2019 . Published Online: 24 June 2019

Giacomo Melani , Yuki Nagata , R. Kramer Campen , and Peter Saalfrank 



View Online



Export Citation



CrossMark

ARTICLES YOU MAY BE INTERESTED IN

Vibrational spectroscopy of hydroxylated α -Al₂O₃(0001) surfaces with and without water: An *ab initio* molecular dynamics study

The Journal of Chemical Physics **149**, 014707 (2018); <https://doi.org/10.1063/1.5023347>

Re-orientation of water molecules in response to surface charge at surfactant interfaces

The Journal of Chemical Physics **151**, 034703 (2019); <https://doi.org/10.1063/1.5066597>

Toward *ab initio* molecular dynamics modeling for sum-frequency generation spectra; an efficient algorithm based on surface-specific velocity-velocity correlation function

The Journal of Chemical Physics **143**, 124702 (2015); <https://doi.org/10.1063/1.4931106>

Lock-in Amplifiers up to 600 MHz

starting at

\$6,210



Zurich
Instruments

Watch the Video 



Vibrational spectra of dissociatively adsorbed D₂O on Al-terminated α -Al₂O₃(0001) surfaces from *ab initio* molecular dynamics

Cite as: J. Chem. Phys. 150, 244701 (2019); doi: 10.1063/1.5099895

Submitted: 12 April 2019 • Accepted: 23 May 2019 •

Published Online: 24 June 2019



View Online



Export Citation



CrossMark

Giacomo Melani,¹  Yuki Nagata,²  R. Kramer Campen,³  and Peter Saalfrank^{1,a)} 

AFFILIATIONS

¹Theoretische Chemie, Institut für Chemie, Universität Potsdam, Karl-Liebknecht-Straße 24-25, D-14476 Potsdam-Golm, Germany

²Max-Planck-Institut für Polymerforschung, Ackermannweg 10, 55128 Mainz, Germany

³Fritz-Haber-Institut der Max-Planck-Gesellschaft, Faradayweg 4-6, D-14195 Berlin, Germany

^{a)}Electronic mail: peter.saalfrank@uni-potsdam.de

ABSTRACT

Water can adsorb molecularly or dissociatively onto different sites of metal oxide surfaces. These adsorption sites can be disentangled using surface-sensitive vibrational spectroscopy. Here, we model Vibrational Sum Frequency (VSF) spectra for various forms of dissociated, deuterated water on a reconstructed, Al-terminated α -Al₂O₃(0001) surface at submonolayer coverages (the so-called 1-2, 1-4, and 1-4' modes). Using an efficient scheme based on velocity-velocity autocorrelation functions, we go beyond previous normal mode analyses by including anharmonicity, mode coupling, and thermal surface motion in the framework of *ab initio* molecular dynamics. In this way, we calculate vibrational density of states curves, infrared, and VSF spectra. Comparing computed VSF spectra with measured ones, we find that relative frequencies of resonances are in quite good agreement and linewidths are reasonably well represented, while VSF intensities coincide not well. We argue that intensities are sensitively affected by local interactions and thermal fluctuations, even at such low coverage, while absolute peak positions strongly depend on the choice of the electronic structure method and on the appropriate inclusion of anharmonicity.

Published under license by AIP Publishing. <https://doi.org/10.1063/1.5099895>

I. INTRODUCTION

Metal oxides in contact with water play an important role in corrosion, electrochemistry, heterogeneous catalysis, and geochemistry.¹⁻⁹ In particular, aluminum oxide surfaces are of interest as model systems for water/metal oxide interfaces.¹⁰ Among the different forms of aluminum oxide, a special focus has been on α -Al₂O₃ (also known as *corundum*) or α -alumina. Despite previous¹¹⁻¹⁶ and very recent works,¹⁷⁻²¹ even for its thermodynamically most stable (0001) surface termination,²² the mechanism of water adsorption, and the resulting adsorbate surface structure, is still an object of much current research. For example, the ratio of dissociative vs molecular adsorption, the type and relative importance of different adsorption sites, the role of surface dosing (e.g., pinhole vs molecular beam dosing), the effect of (pre)coverage, the surface reactivity under ambient conditions, and the role of surface defects and

of the chemical composition of the uppermost surface layer (e.g., aluminum- vs oxygen-terminated or hydroxylated) are still under dispute.

To shed light on these aspects, we have combined experimental and theoretical studies of the adsorption of water at *low coverages* on α -Al₂O₃ surfaces, either α -Al₂O₃(0001) in Al-terminated or hydroxylated forms,^{17,23-27} or other surfaces such as the O-terminated α -Al₂O₃(1102) and α -Al₂O₃(1120). In the experiment, surface-sensitive Vibrational Sum Frequency (VSF) generation spectroscopy^{15,28-32} was used to probe OH (or OD) and AlO vibrations, supported by theoretical interpretation. For instance, in Refs. 23 and 24, H₂O adsorption on the Al-terminated (0001) surface was studied by periodic Density Functional Theory (DFT). To be more specific, the Al-I terminated (0001) surface is thermodynamically the most stable one under Ultrahigh Vacuum (UHV) conditions,²² whereas under “moist” conditions on a longer time scale

(of days), the so-called hydroxylated O-terminated surface, which is saturated by (Al)-OH bonds, becomes the dominant one. In Refs. 23 and 24, different H₂O adsorption structures on the Al-I terminated (0001) surface were identified by DFT: a molecularly adsorbed state and various forms of dissociated water. At submonolayer coverages (one water per 2×2 unit cell, i.e., coverage 1/4), a water molecule was found to coordinate with O-down to an unsaturated surface-Al atom (a “Coordinatively Unsaturated Site,” CUS), while in dissociative cases a water molecule splits into OH (or OH⁻) sitting on an Al CUS site and H (or H⁺) attaching either to the nearest (“1-2 dissociation”) or a next-nearest neighbor surface O atom (“1-4 dissociation”) or to an O atom even farther away (“1-4’ dissociation”)—see Figs. 1(a)–1(c) below. In Refs. 17, 23, and 24, it was argued that a molecular adsorbate is metastable with respect to dissociation into 1-2 (the most stable) and 1-4 species (of about the same stability as the molecular species). By hydrogen diffusion, out of 1-4 also the form 1-4’ (slightly less stable than 1-4) could be formed. In Refs. 17, 23, and 24, the 1-2 and 1-4 species, which had already been postulated theoretically long time ago,^{11,14} were investigated and finally observed experimentally, together with 1-4’ species. In the experiment,²⁴ D₂O had been dosed on the α -alumina (0001) surface with a molecular beam source (MBS), leading to a low-coverage situation (see below), and the reaction products were spectroscopically identified by VSF. VSF signals corresponded to six distinct OD stretch vibrations: three for the “surface OD” bonds of 1-2, 1-4, and 1-4’, and three for the “adsorbate OD” bonds of them. Here, “surface OD” refers to the vibration of the D(+)-surface O vibration, while “adsorbate OD” refers to the vibration

of the dissociated OD(–) fragment of water, on the Al CUS site. The modes, which will be reiterated below, were assigned based on vibrational frequencies obtained by Normal Mode Analysis (NMA) using DFT, i.e., on the harmonic approximation. Anharmonicity, if at all, was only treated along normal modes, while intermode coupling and finite temperature effects (leading to molecular motion and line broadening) were not considered, and also no VSF intensities were computed. While NMA yielded relative frequencies in reasonable agreement with the experiment, in this work we go beyond the previous, static, theoretical treatment both to assess the importance of these additional effects and to calculate intensities and linewidths. In particular, using Born-Oppenheimer *Ab Initio* Molecular Dynamics (AIMD), we shall account for molecular motion, anharmonicity, and mode couplings at finite temperature, and we will determine VSF intensities using a correlation function approach. This serves to get insight into the mentioned, so far neglected effects and to critically assess the mode assignment done in Ref. 24.

In fact, even if the vibrational peaks retrieved in the experiment could be reasonably associated with calculated OD frequency spacings from the suggested adsorption structures above, there was quantitative disagreement in frequencies and some peculiar values within the measured frequencies could be noticed. For instance, Kirsch and co-workers reported VSF resonances at high frequency centered around 2900 cm^{-1} , corresponding to “surface OD” vibrations.²⁴ These very high vibrational frequencies do not fall in the typical OD stretching range known for hydroxyl groups on aluminum oxides, at least on aluminum oxide clusters such as Al₃O₄⁺

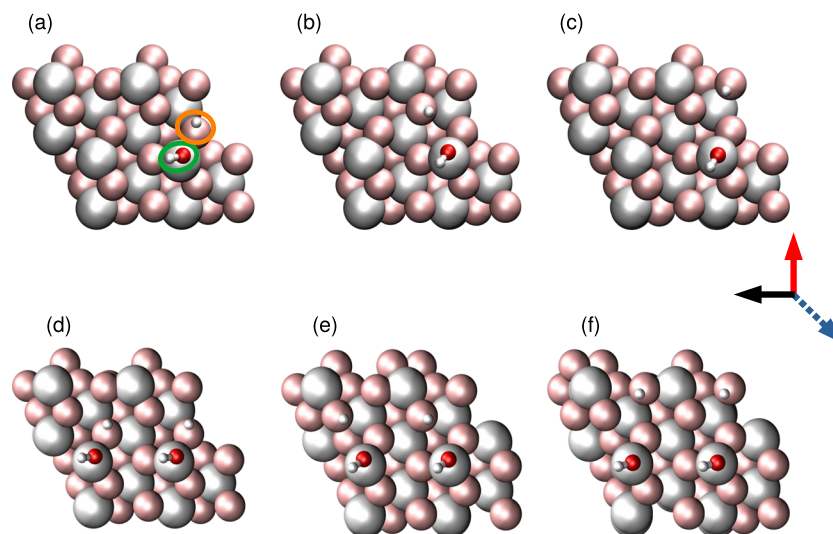


FIG. 1. Top views of the dissociated D₂O species on the Al-terminated α -Al₂O₃(0001) (2×2) surface, used as starting geometries for AIMD. Dissociated species for coverage 1/4 (one water molecule per cell) are in the upper panels: (a) 1-2 monomer, (b) 1-4 monomer, and (c) 1-4’ monomer. The lower panels show specific dimer models, for coverage 1/2 (two water molecules per cell): (d) 1-2 dimer, (e) 1-4 dimer, and (f) 1-4’ dimer. All models consist of 9-layer surface supercells with additional water on top of the uppermost (Al) layer, with stoichiometric compositions of Al₂₄O₃₆ D₂O and Al₂₄O₃₆(D₂O)₂ for monomer and dimer cases, respectively. Optimized PBE+D2 structures are shown, with surface atoms visualized as “van der Waals spheres” in pale, while dissociated water molecules are shown in “ball-and-stick” representation (D in white, Al in gray, and O in red). In what follows, the water-hydroxyl groups are also denoted as “adsorbate OD” (circled in green), while OD groups consisting of a water-D plus a substrate O will be denoted as “surface OD” (circled in orange). For later reference, the Cartesian coordinate system used in this work is given by red (x-axis), black (y-axis), and blue (z-axis) arrows, the former in the surface plane and the latter perpendicular and pointing away from it.

in contact with water.³³ In Ref. 19, the occurrence of “surface OH” vibrations after H₂O adsorption on both single-crystal α -alumina and metal oxide particles was questioned by InfraRed (IR) spectroscopy. Furthermore, in recent AIMD simulations of an MBS experiment for water scattering at Al-terminated α -alumina (0001),¹⁷ it was found that only with refined models for the water molecular beam (e.g., with rovibrational excitation or cluster formation) and/or the alumina surface (thermalized surface, preadsorption), the three proposed products of D₂O dissociation²⁴ could be retrieved. All of this shows that indeed, a closer look into the molecular dynamics of low-coverage water on α -alumina (0001) with emphasis on vibrational spectra simulation is highly desirable.

We note that a very similar approach has been followed recently by us for VSF spectra of water on the *hydroxylated* O-terminated α -Al₂O₃(0001) surface, at somewhat higher water coverages (of up to two monolayers).¹⁸ Independent of that, DelloStritto *et al.* used AIMD-based correlation functions to compute VSF spectra for hydroxylated α -Al₂O₃(0001) and α -Al₂O₃(11 $\bar{2}$ 0) surfaces at even higher (basically bulk) water loads.^{20,34} In Refs. 18, 20, and 34, a good match to existing experiments was found, which shows that the present AIMD/correlation function methodology seems to be well-suited for exploring water-covered alumina surfaces.

The paper is organized as follows. In Sec. II, we present different strategies to calculate vibrational spectra from DFT/AIMD. In particular, efficient methods based on velocity-velocity correlation functions will be adopted to compute Vibrational Density Of States (VDOS), IR, and VSF spectra. In Sec. III, computational models for the three main *dissociated* species (1-2, 1-4, and 1-4') will be developed, which serve as starting geometries for AIMD simulations for two low coverages (1/4 and 1/2). Numerical details of the stationary calculations and of AIMD will be provided. In Sec. IV, we first compare stationary calculations (including geometry optimizations and normal mode analyses) with AIMD simulations, for the three different starting configurations. Then, vibrational signatures will be provided in the form of computed VDOS, IR, and VSF signals. The latter will be critically compared to experimental findings. Section V summarizes and concludes this work.

II. COMPUTATION OF VIBRATIONAL SPECTRA: METHODS

The simplest route toward modeling of adsorbate vibrations from *first principles* is to perform a normal mode analysis of the geometry-optimized system. NMA frequencies, however, give no information on anharmonicity, mode coupling, and line intensities or widths in vibrational spectroscopy. A step beyond NMA is to compute the vibrational density of states (VDOS) from the Fourier transform of a velocity-velocity autocorrelation function (VAAF) obtained from (AI)MD,^{35,36}

$$\text{VDOS}(\omega) \propto \sum_{i=1}^N \int_0^{\infty} \langle \underline{v}_i(0) \cdot \underline{v}_i(t) \rangle e^{-i\omega t} dt. \quad (1)$$

Here, $\underline{v}_i(t)$ is the velocity of atom i at time t and N is the total number of moving atoms. $\langle \underline{v}_i(0) \cdot \underline{v}_i(t) \rangle$ is the velocity-velocity autocorrelation function, in this case averaged over different trajectories. The VDOS accounts for anharmonicity, dynamical broadening, and

also thermal effects. Below, VDOS curves will be computed by using AIMD based on periodic DFT, for canonical (finite temperature) ensembles of the systems under study.

Classical molecular dynamics trajectories can provide direct access to vibrational spectra such as IR and VSF, employing other correlation functions according to linear response theory,^{20,34,37–44} where mode intensities and selection rules are properly taken into account. An IR spectrum is related to the first-order optical susceptibility, $\chi_{ab}^{(1)}$, which can be calculated from the Fourier transform of the dipole-dipole autocorrelation function,

$$\chi_{ab}^{(1)}(\omega) \propto i \int_0^{\infty} \langle \mu_a(0) \mu_b(t) \rangle e^{-i\omega t} dt. \quad (2)$$

Here, a, b denote Cartesian coordinates x, y, z , with z being the direction perpendicular to the surface plane and x and y being directions parallel to it (see below). $\mu_{a/b}(t)$ is the a/b th component of the dipole moment at time t and $\langle \dots \rangle$ is an ensemble average. An IR spectrum with light polarized along the z direction is then obtained from the real part of the susceptibility as $I_z^{\text{IR}}(\omega) \propto \text{Re}\{\chi_{zz}^{(1)}(\omega)\}$. By the various polarizations, experiments with s - and p -polarized light may be simulated, i.e., with field component parallel (“ p ”) and perpendicular (“ s ,” “*senkrecht*”) to the plane of the incoming light waves.

VSF spectra can also be related to a classical correlation function, by calculating the second-order susceptibility $\chi_{abc}^{(2)}$. As pioneered by Morita and co-workers,^{45–49} this one can be extracted from (AI)MD calculations as

$$\chi_{abc}^{(2)}(\omega) \propto i \int_0^{\infty} \langle \mu_c(0) \alpha_{ab}(t) \rangle e^{-i\omega t} dt. \quad (3)$$

Now, $\alpha_{ab}(t)$ is the ab -component of the polarizability tensor $\underline{\alpha}$ at time t , entering with the dipole component μ_c the averaged cross correlation function $\langle \mu_c(0) \alpha_{ab}(t) \rangle$. As for the $\chi_{ab}^{(1)}$, indices a, b , and c correspond to Cartesian components in the molecular reference frame. In VSF spectroscopy, nonresonant and resonant parts, the latter given by (3), contribute to an effective susceptibility $\chi_{\text{eff},abc}^{(2)}(\omega)$, and several tensor elements (multiplied by Fresnel factors) determine the signal. In this work, we concentrate on so-called *ssp*-polarization, by modeling the VSF signal as $I_{\text{spp}}^{\text{VSF}}(\omega) \propto |\chi_{xxz}^{(2)}|^2$. The notion *ssp* means that incoming IR light is p -polarized, while the visible light and the outgoing signal are both s -oriented.

In DFT-based AIMD simulations, the evaluation of dipole moments and polarizabilities can be performed “on the fly” by means of computationally expensive routes, for instance, involving Maximally Localized Wannier Functions (MLWFs).^{50,51} These methods allow for a direct use of Eqs. (2) and (3) but usually require long trajectories (hundreds of picoseconds) because of slow convergence of the time correlation function in Eq. (3).^{40,42} In order to achieve convergence together with reasonable computational cost, computationally inexpensive schemes are highly desirable. In this work, we use the developments by Ohto *et al.*, which employ a (parameterized) approximation for the OH(D) polarizability and dipole moment;⁴² only a subset of the velocity-velocity autocorrelation function (VAAF) is computed in the end to determine $\chi_{ab}^{(1)}(\omega)$ and $\chi_{abc}^{(2)}(\omega)$. Note that similar approaches have also been reported

in the literature to calculate VSF spectra of aqueous interfaces from AIMD.^{52,53}

In the VVAF method⁴² for OD stretching vibrations, M OD oscillators are considered. The dipole moment of oscillator i , $\underline{\mu}_i(t)$, is approximated as the sum of a permanent part and a dynamical part proportional to the displacement of the OD bond out of equilibrium, i.e., the bond dipole moment is linearly approximated. Under these approximations, and by considering a quantum correction factor $Q(\omega) = \frac{\hbar\omega}{k_B T} / (1 - e^{-\frac{\hbar\omega}{k_B T}})$, with T as the temperature and k_B as Boltzmann's constant, one obtains for the first-order susceptibility

$$\chi_{ab}^{(1)}(\omega) = \frac{Q(\omega) \mu'_{OD}(\omega)^2}{i\omega^2} \int_0^\infty \sum_i^M \sum_j^M \langle v_{bj}^{OD}(0) v_{ai}^{OD}(t) \rangle e^{-i\omega t} dt. \quad (4)$$

Here, $v_{a,i} = \dot{r}_{a,i}$ is the a th component ($=x, y, z$) of the velocity vector of OD bond i , i.e., the time-derivative of the coordinate vector $\underline{r}_i(t) = (x_i(t), y_i(t), z_i(t))$ of that bond. Similarly, the second-order susceptibility can be recast as⁴²

$$\chi_{abc}^{(2)}(\omega) = \frac{Q(\omega) \mu'_{OD}(\omega) \alpha'_{OD}(\omega)}{i\omega^2} \times \int_0^\infty \sum_i^M \sum_j^M \left\langle v_{c,i}^{OH}(0) \frac{v_j^{OD}(t) r_j^{OD}(t)}{|r_j^{OD}(t)|} \right\rangle e^{-i\omega t} dt \quad (5)$$

if $a = b$, $\chi_{abc}^{(2)}(\omega) = 0$, otherwise. Derivatives of dipole moments and polarizabilities with respect to the vibrational coordinate, $\mu'_{OD}(\omega)$ and $\alpha'_{OD}(\omega)$, are calculated from parameters derived by Skinner and co-workers for OH(D) bonds in an aqueous environment,^{54,55} as

$$\mu'_{OD}(\omega) = \left(A_\mu + \frac{B_\mu(C - \omega)}{D} \right) \mu'_{OD,g}, \quad (6)$$

$$\alpha'_{OD}(\omega) = \left(A_\alpha + \frac{B_\alpha(C - \omega)}{D} \right) \alpha'_{OD,g}, \quad (7)$$

where $A_\mu = 1.377$, $B_\mu = 53.03$, $A_\alpha = 1.271$, $B_\alpha = 6.287$, $C = 2745.8 \text{ cm}^{-1}$, and $D = 4870.3 \text{ cm}^{-1}$. Furthermore, $\mu'_{OD,g}$ and $\alpha'_{OD,g}$ are gas phase values (no environment), and ω is the frequency in wavenumbers. The values of $\mu'_{OD,g}$ and $\alpha'_{OD,g}$ are not needed here because we are interested in relative spectra and the intensities are given in "arbitrary units."

The use of Eqs. (4) and (5) requires knowledge of all OD bonds and their corresponding velocity vectors, which can be obtained from AIMD, and the parameterizations (6) and (7). The method proposed in Ref. 42 avoids costly "on the fly" calculations of μ' and α' , and it has been demonstrated to be transferable to other aqueous systems, e.g., to the $\text{H}_2\text{O}/\text{TiO}_2$ and $\text{H}_2\text{O}/\text{graphene}$ interfaces.^{53,56} We have employed the very same approach, with parameters for OH instead of OD, to calculate vibrational spectra (VDOS, IR, and VSF) of hydroxylated α -alumina (0001) with and without additional water in Ref. 18.

III. COMPUTATIONAL MODELS AND THEIR REALIZATION

A. Static and AIMD DFT calculations

In order to characterize frequencies of adsorbed D_2O on the Al-terminated α - Al_2O_3 (0001) surface, we performed geometry optimizations for selected supercell models, NMA and AIMD simulations at the Kohn-Sham⁵⁷ DFT (KS-DFT) level of theory, employing the Perdew-Burke-Ernzerhof (PBE)⁵⁸ exchange-correlation functional and a projector-augmented plane-wave (PAW) basis⁵⁹ as implemented in the Vienna *Ab initio* Simulation Package (VASP).⁶⁰⁻⁶² van der Waals interactions were included by Grimme's empirical D2 method.⁶³ For all calculations, a $3 \times 3 \times 1$ k-point mesh and a kinetic energy cutoff of 400 eV were used.

When calculating vibrational modes within NMA, no frequency rescaling was performed unless stated otherwise. We performed AIMD simulations within the canonical ensemble (NVT) at 300 K using the Nosé-Hoover thermostat.⁶⁴ We started our AIMD trajectories from optimized PBE+D2 structures of dissociated species, as shown in Fig. 1. Initial velocities were generated randomly according to a Boltzmann distribution at $T = 300$ K. The equations of motion for nuclear degrees of freedom were propagated according to the Velocity-Verlet algorithm with a time step of $\Delta t = 0.2$ fs. We ran simulations for 50 ps in total. Technically, this was done by running five trajectories for each system, each of them being 10 ps long. Most of the propagation time was used for thermal equilibration, and only the last segment of each trajectory has been employed to sample the correlation functions in an interval $[0, t_{\text{samp}}]$. Different sampling times t_{samp} have been tested. All the results shown below are for $t_{\text{samp}} = 2$ ps, leading to a formal VDOS spectral resolution of about 17 cm^{-1} .

The velocity-velocity autocorrelation function $G(t) = \sum_{i=1}^N \langle \underline{v}_i(0) \underline{v}_i(t) \rangle$, whose Fourier transform gives the VDOS according to Eq. (1), was evaluated as³⁶

$$G(t) = \frac{1}{N_t} \sum_{i=1}^N \sum_{j=1}^{N_t} \langle \underline{v}_i(t_j) \cdot \underline{v}_i(t_j + t) \rangle. \quad (8)$$

Here, $N_t = 1 + t_{\text{samp}}/\Delta t$ is the number of time steps used for sampling, and $t_j = (j - 1)\Delta t$ ($j = 1, \dots, N_t$), while N is the total number of atoms in the system. The correlation functions were evaluated at the same time steps t as those used for the AIMD. Again, $\langle \underline{v}_i(t_j) \cdot \underline{v}_i(t_j + t) \rangle$ defines an average over all AIMD trajectories. Other correlation functions needed in this work were evaluated accordingly. Finally, for Fourier transforms, we multiply all (auto)correlation functions by Hann window functions

$$w(t) = \cos^2\left(\frac{\pi t}{2t_{\text{samp}}}\right), \quad (9)$$

and the time integrals are done from 0 to t_{samp} . For further numerical details, see Ref. 18.

B. Computational models

In what follows, low-coverage situations for water on Al-terminated α - Al_2O_3 (0001) are studied. We use the Al-I surface model,²² the same as in Refs. 17, 21, 23, and 24, comprising a

9-atomic layer (2×2) supercell (layer sequence $\text{Al}_4\text{-O}_{12}\text{-Al}_4\text{-Al}_4\text{-O}_{12}\text{-Al}_4\text{-Al}_4\text{-O}_{12}\text{-Al}_4$) with dimensions $9.66 \text{ \AA} \times 9.66 \text{ \AA} \times 31.41 \text{ \AA}$ (20 \AA of vacuum in the z -direction) and employing 3D periodic boundary conditions. For geometry optimizations, NMA and AIMD, the lowest four layers ($\text{Al}_4\text{-O}_{12}\text{-Al}_4\text{-Al}_4$) are kept fixed at the bulk values optimized in Ref. 24, while the upper five layers ($\text{O}_{12}\text{-Al}_4\text{-Al}_4\text{-O}_{12}\text{-Al}_4$) are allowed to be relaxed or to move. On top of this relaxed surface, which exhibits four Al CUS sites, water molecules are adsorbed and corresponding structures have been optimized.

Two coverages were considered. In a first model, we have one water molecule per (2×2) cell, i.e., coverage 1/4. This coverage is “low” but still higher than in the experiment. For the 1/4 coverage case, the corresponding, most stable dissociated species are those of Refs. 17, 21, and 24, i.e., the 1-2, 1-4, and 1-4' configurations shown in Figs. 1(a)–1(c). The molecular adsorbate corresponds also to a local minimum but is not shown here. In Table I, we list adsorption energies $E_{\text{ads}} = E(\text{adsorbate} + \text{surface}) - [E(\text{adsorbate}) + E(\text{surface})]$ for dissociated and the molecular species obtained with PBE+D2, along with the corresponding adsorption free energies $G_{\text{ads}} = H_{\text{ads}} - TS_{\text{ads}}$ at $T = 300 \text{ K}$. Adsorption free energies were calculated in harmonic oscillator/ideal gas approximation as detailed in Ref. 23, now for D_2O rather than H_2O .

From the table, we can see that each dissociation mode (1-2, 1-4, 1-4') comprises two OD groups, a water-hydroxyl group which we denote as “adsorbate OD” in what follows and an OD group consisting of a water-D plus a substrate O, “surface OD.” 1-2 is most stable, 1-4 and the molecular species are less but about equally stable on this level of theory, and 1-4' is slightly less stable than all the previous ones, in agreement with previous observations.²⁴

In order to study the effects of coverage, also the case with two molecules per (2×2) cell was considered, i.e., coverage 1/2. Various combinations of dissociated and molecular adsorbed species and their adsorption sites are now conceivable. In Fig. 1, we show PBE+D2 optimized structures obtained by simply doubling the optimized 1-2, 1-4, and 1-4' motifs of the monomer at a neighboring Al CUS site and reoptimizing. In this case, doubly dissociated species are obtained which will be used later as starting geometries for AIMD. We emphasize, however, that these doubly dissociated dimer species are not necessarily the lowest-energy structures. While looking at the effect of surface coverage is certainly of interest, a full configurational sampling of adsorption geometries was not the aim of

TABLE I. PBE+D2 adsorption energies and Gibbs free energies (at 300 K) for adsorption of D_2O on $\alpha\text{-Al}_2\text{O}_3(0001)$, at two different coverages. The values for dimers were divided by two, so they are reported as adsorption energies per D_2O molecule. All energies are in eV.

Species	Monomer		Dimer	
	E_{ads}	$G_{\text{ads}} (T = 300 \text{ K})$	E_{ads}	$G_{\text{ads}} (T = 300 \text{ K})$
Molecular	−1.31	−1.18
1-2	−1.69	−1.57	−1.68	−1.55
1-4	−1.30	−1.18	−1.21	−1.10
1-4'	−1.21	−1.10	−1.33	−1.22

this work. In fact, during AIMD (at $T = 300 \text{ K}$) in some cases, “mixed configurations” were formed with one dissociated and one molecular adsorbate (see below). This requires a proton/deuteron transfer to form an intact water molecule, out of a dissociated species. For the example of the dissociated “1-4 dimer” in Fig. 1(e), the formation of such a mixed dimer was studied in Appendix A by computing a reaction path for hydrogen transfer using the nudged elastic band method.^{65,66} There it is shown that indeed, the mixed species is by about 0.4 eV (0.2 eV per molecule) more stable than the doubly dissociated species and that the activation energy for this process is very small (less than 0.05 eV), suggesting a fast reaction. In fact, also in AIMD simulations of molecular beam scattering events, the formation of mixed species was seen.¹⁷ From Table I, we note that the adsorption energies/free energies per water molecule of the dimers differ by about 0.1 eV the most from the monomers, indicating only weak interactions between the two water adsorbates in the dimer case for the starting configurations shown in Fig. 1. Interestingly, however, now the 1-4' configuration appears to be more stable than 1-4, i.e., the stability order between these two appears to be reversed.

IV. RESULTS AND DISCUSSION

A. Vibrational frequencies from normal mode analysis

As a first step toward the characterization of vibrational modes for different dissociated D_2O structures on Al-terminated α -alumina (0001), we report calculated frequencies by NMA using PBE+D2 treatment at the optimized geometries of Fig. 1. Since our main source of comparison is VSF experiments from Ref. 24, we list only OD-stretching modes in Table II. We also show experimental values and corresponding assignments,²⁴ as well as differences $\Delta\tilde{\nu} = \tilde{\nu} - \tilde{\nu}(\text{OD}_{\text{surf}}^{1-2})$ relative to the lowest-energy OD vibration, $\text{OD}_{\text{surf}}^{1-2}$.

Our calculated NMA wavenumbers $\tilde{\nu}$ for coverage 1/4 reproduce the harmonic values reported in Ref. 24, obtained at the same level of theory (with slightly different computational settings). As noticed there, there is a consistent and systematic red-shift of about 100 cm^{-1} of the theoretical OD-stretches compared to the experimental ones. If we include anharmonicity along the normal modes in a quantum mechanical fashion (but no mode coupling) as done in Ref. 24, we get the values “AHO” (anharmonic oscillator) shown in the table. These indicate that the red-shift from the experiment becomes even larger. However, we note that spacings between resonances (measured by $\Delta\tilde{\nu}$) are quite similar between NMA/AHO theory and experiment, which was the basis for mode assignment in Ref. 24. In particular, there are large frequency spacings between “adsorbed OD” and “surface OD” vibrations, with the latter being less energetic. Referring to the mismatch in absolute wavenumbers, we mention that a significant improvement of OD stretching frequencies is achieved if scaling factors are used. Using a scaling factor of 1.031 as recommended for PBE in Ref. 67, the harmonic frequencies for the “monomer” case become 2710 ($\text{OD}_{\text{surf}}^{1-2}$), 2729 ($\text{OD}_{\text{surf}}^{1-4}$), 2770 ($\text{OD}_{\text{surf}}^{1-4'}$), 2875 ($\text{OD}_{\text{ads}}^{1-4}$ and $\text{OD}_{\text{ads}}^{1-4'}$), and 2891 ($\text{OD}_{\text{ads}}^{1-2}$). This brings absolute measured and theoretical frequencies much closer together up to $\sim 20\text{--}35 \text{ cm}^{-1}$.

We also learn from Table II that at the higher coverages NMA frequencies do not change much, at least for the simple models shown in Figs. 1(d)–1(f). Each mode splits into two (symmetric and

TABLE II. Comparison between vibrational (stretching) wavenumbers $\tilde{\nu}$ at the DFT/PBE+D2 level of theory and experimental results from Ref. 24 for dissociated D₂O on Al-terminated α -Al₂O₃(0001). $\Delta\tilde{\nu} = \tilde{\nu} - \tilde{\nu}(\text{OD}_{\text{surf}}^{1-2})$ gives resonance positions, relative to the lowest-frequency vibration, OD_{surf}¹⁻². All wavenumbers are in cm⁻¹. Subscripts “surf” and “ads” denote “surface OD” and “adsorbate OD” as specified in the text. The theoretical values are for NMA (normal mode analysis), AHO (anharmonic oscillator treatment), and VDOS (vibrational density of states), the latter obtained from AIMD at 300 K.

Assignment	Expt. ^a		Theory, monomer						Theory, dimer		
			NMA		AHO ^a		VDOS		NMA		VDOS
	$\tilde{\nu}$	$\Delta\tilde{\nu}$	$\tilde{\nu}$	$\Delta\tilde{\nu}$	$\tilde{\nu}$	$\Delta\tilde{\nu}$	$\tilde{\nu}_{\text{max}}$	$\Delta\tilde{\nu}$	$\tilde{\nu}$	$\tilde{\nu}_{\text{max}}$	$\Delta\tilde{\nu}$
OD _{surf} ¹⁻²	2729 ± 5	0	2629	0	2523	0	2596	0	2628, 2629	2607	0
OD _{surf} ¹⁻⁴	2764 ± 5	35	2647	18	2541	18	2636	40	2618, 2624
OD _{surf} ^{1-4'}	2790 ± 3	61	2687	58	2583	60	2649	53	2693, 2694	2682	75
OD _{ads} ¹⁻⁴	2900 ± 7	171	2789	160	2696	171	2781	185	2780, 2781	2778	171
OD _{ads} ^{1-4'}	2900 ± 7	171	2789	160	2697	174	2780	184	2787, 2787	2778	171
OD _{ads} ¹⁻²	2910 ± 7	181	2804	175	2713	190	2795	199	2792, 2793	2788	181

^aFrom Ref. 24.

^bBroad VDOS in this region.

antisymmetric), with only small splittings (in the order of 1 cm⁻¹) and hardly shifted with respect to the monomer cases—the “1-4 surf” case being an exception.

B. Vibrational density of states from AIMD

In order to go beyond static DFT, we now report the results on VDOS curves calculated from AIMD trajectories at constant temperature (300 K). In Fig. 2, we show the VDOS for the three dissociated species in the “monomer” (coverage 1/4) and “dimer” (coverage 1/2) models when used as respective starting configurations in AIMD. In the upper panels of Fig. 2, VDOS curves over a frequency

range from 0 to 3000 cm⁻¹ are shown, while the lower panels refer to the OD stretching region only between 2500 and 3000 cm⁻¹.

It appears that the spectra for both triads of reaction products have two main bands. Up to 1000 cm⁻¹ surface vibrations and OD bending modes are involved, while above 2500 cm⁻¹ we see the signatures of different OD oscillators. For the “monomer” dissociated species, we have two maxima per model (1-2, 1-4, or 1-4'), i.e., we retrieve all six modes reported in Table II. In the column “monomer, VDOS,” we show the maxima of the VDOS curves as $\tilde{\nu}_{\text{max}}$. Compared to the NMA results, we notice frequency shifts to lower values for all modes: the OD_{ads} vibrations are red-shifted by between 8 cm⁻¹ for OD_{ads}¹⁻⁴ and 38 cm⁻¹ for OD_{surf}^{1-4'}. In general,

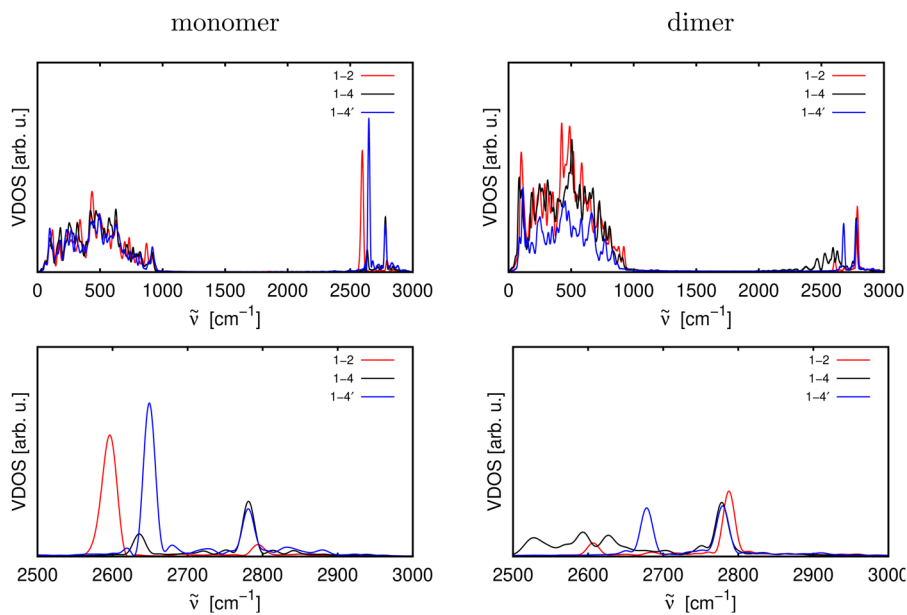


FIG. 2. VDOS curves obtained by AIMD at 300 K, using the dissociated species 1-2, 1-4, and 1-4' for “monomers” (left) and “dimers” (right) of Fig. 1 as starting configurations. Upper panels show the frequency range [0, 3000] cm⁻¹, and lower panels show the OD stretching region [2500, 3000] cm⁻¹. In the right panels, the VDOS scale is half that of the scale in the left panels.

red-shifts are larger for “surface OD” than for “adsorbed” fragments. The red-shifts arise from anharmonicity of the potential (including an approximate treatment of mode coupling). Note that, due to the absence of vibrational energy quantization and zero-point energy, in classical dynamics only the low-energy portion of the potential is probed at 300 K, and therefore, anharmonic corrections are underestimated with respect to a quantum treatment (AHO)—for which a red-shift $\sim 100\text{ cm}^{-1}$ was found above.

For the “dimer,” coverage 1/2 dissociative D_2O adsorption structures (right panels in Fig. 2), a rather similar behavior compared to the unimolecular example is found. Again, VDOS peaks at high frequency are comparable to NMA frequencies, with a red-shift of OD stretches by $\sim 10\text{ cm}^{-1}$ for OD_{ads} and by $\sim 20\text{ cm}^{-1}$ (at most) for OD_{surf} bonds. The frequencies for maxima in the VDOS are also shown in Table II. No value has been given for $\text{OD}_{\text{surf}}^{1-4}$, however, because around 2600 cm^{-1} a broad distribution of frequencies with several, comparably intense maxima is found. This has to do with a peculiar effect, not observed for other structures: in two of the five trajectories, we propagated for the 1-4 dimer, a deuterium atom moved from a “surface” configuration to an “OD adsorbate” unit, forming a molecularly adsorbed D_2O species. In fact, as mentioned in Sec. III and in Appendix A, we find a mixed structure with one molecular and one dissociated water molecule being more stable, at least for 1-4. As a consequence, also molecular species show up in the VDOS. In Ref. 24, a normal mode analysis for a single D_2O molecule on a (2×2) cell of $\alpha\text{-Al}_2\text{O}_3(0001)$ gave symmetric and antisymmetric D_2O stretch vibrations of 2550 and 2664 cm^{-1} , respectively, i.e., below and above the $\text{OD}_{\text{surf}}^{1-4}$ vibrational frequency of 2647 cm^{-1} (cf. Table II).

In general, the VDOS curves reflect the thermal motion of the adsorbates. This gives rise to new signals beyond NMA (most notably for the “1-4 dimer”) and to broadening of peaks beyond the energy resolution imposed by the finite propagation time. These effects will be analyzed in more detail in Secs. IV C and IV D.

C. IR spectra from NVT/AIMD simulations

In this section, we calculate IR spectra using AIMD at 300 K and adopting different polarization axes a , i.e., $I_a^{\text{IR}}(\omega) \propto \text{Re}\{\chi_{aa}^{(1)}(\omega)\}$, for $a = x, y$, and z . Again, z is the direction perpendicular to the substrate, and x and y are orthogonal directions in the surface plane, as defined in the caption of Fig. 1. The different polarization directions serve to model differently polarized IR experiments (i.e., s - and p -polarization) and also improve insight into the nature of the sampled vibrational modes.

Let us consider the z -polarized spectrum of the “monomer” case first (lowest left panel in the figure), which can be considered as representative for a p -polarized IR spectrum. We see six peaks corresponding to the six different OD vibrations, at positions very close to those found in the VDOS spectra as listed in Table II. Both for 1-2 and 1-4', the lower-energy “surface OD” vibrations show a higher intensity than the “adsorbate OD” intensities, while for 1-4 it is the other way round. We assume that the intensity order observed for 1-2 and 1-4' is a consequence of the fact that the amplitude of the z -component of the transition dipole moment is larger for the “surface OD” than for the “adsorbate OD” vibrations. This indicates smaller polar angles θ , between the “surface OD” bond and the surface normal (the z -direction), than “adsorbate OD.” In fact, the

optimized structures of Fig. 1 give $\theta = 37^\circ, 26^\circ$, and 29° for $\text{OD}_{\text{surf}}^{1-2}$, $\text{OD}_{\text{surf}}^{1-4}$, and $\text{OD}_{\text{surf}}^{1-4'}$, respectively, and $49^\circ, 45^\circ$, and 53° for $\text{OD}_{\text{ads}}^{1-4}$, $\text{OD}_{\text{ads}}^{1-4'}$, and $\text{OD}_{\text{surf}}^{1-2}$, respectively. As shown in Appendix B, during the AIMD runs, θ -distributions are formed, with similar mean θ values, $\langle\theta\rangle = 37^\circ, 30^\circ, 35^\circ$ for “surface OD” and $\langle\theta\rangle = 53^\circ, 54^\circ, 58^\circ$ for “adsorbate OD,” respectively. Hence, the “surface OD” groups are more upright than the “adsorbate OD,” both in the static and dynamic pictures. Besides, not only the average orientation but also the distribution of θ -angles and the mobility of different OD groups are of importance for their spectral response and dependent on the adsorption geometry. As outlined in Appendix B, analysis of the AIMD trajectories shows that for the 1-2 geometry steric hindrance seems to dominate the orientation and dynamic flexibility of OD bonds, while in the 1-4' structure we observe an opposite behavior, with the two bonds acting as almost “free.” An intermediate situation is found for the 1-4 adsorption geometry, where the formation of fluctuating hydrogen bonds seems to introduce a degree of correlation within their angular motion. These observations may provide an explanation for the special ordering of IR z -peak intensities, especially for the 1-4 example. Furthermore, we note that the same intensity ordering as for I_z^{IR} is also found in the VDOS curve of Fig. 2, lower left panel. We conclude that the z -polarized modes contribute dominantly to the vibrational response in p -polarized measurements.

The x - and y -polarized spectra, which can be related to s -polarized IR signals, are more complicated. First of all, we see that different polarizations lead to different spectral behavior. The x - and y -polarized spectra are less intense than the z -polarized ones (the intensity scale of z is two and four times more extended than x and y , respectively, see the caption of Fig. 3). Furthermore, for x - and y -polarization, we see that most of the spectra become much more structured than for z -polarization, with additional peaks showing up, even in frequency regions very close to 2900 cm^{-1} . Such high frequency modes can be associated with OD_{ads} stretching vibrations oriented parallel to the surface plane. We also see large differences between x - and y -polarization. For instance, for the 1-2 dissociated species, the $\text{OD}_{\text{surf}}^{1-2}$ peak around 2600 cm^{-1} is very pronounced in x -polarization and has basically vanished under y -polarization. For the lateral polarizations (in particular, y), we see a tendency that higher-frequency signals, typically associated with “adsorbate OD” groups, gain intensity with respect to the lower-frequency “surface OD” peaks. This may be attributed to the higher flexibility of the former, with respect to motions in the surface plane, compared to the latter. In fact, as one can intuitively expect, the “adsorbate OD” groups can rotate more freely around an azimuthal angle, ϕ , as shown in Fig. 6 of Appendix B. There, very broad distributions $P(\phi)$ are found for the “adsorbate OD” groups, while those of the “surface OD” are more narrow.

We now analyze the IR spectra of “dimer” dissociated structures, which are shown in the right column of Fig. 3. For z -polarization, we find similar peaks to those of the monomer case, albeit with different (relative) intensities and with 1-4 behaving somewhat special again, due to the formation of molecular water in some of the trajectories. The peculiarity of the 1-4 species shows up even more in the x - and y -polarized spectra, exhibiting many peaks, also in the low-energy region at 2500 cm^{-1} (and below), where otherwise no signals were found. In the x -polarized spectrum, also

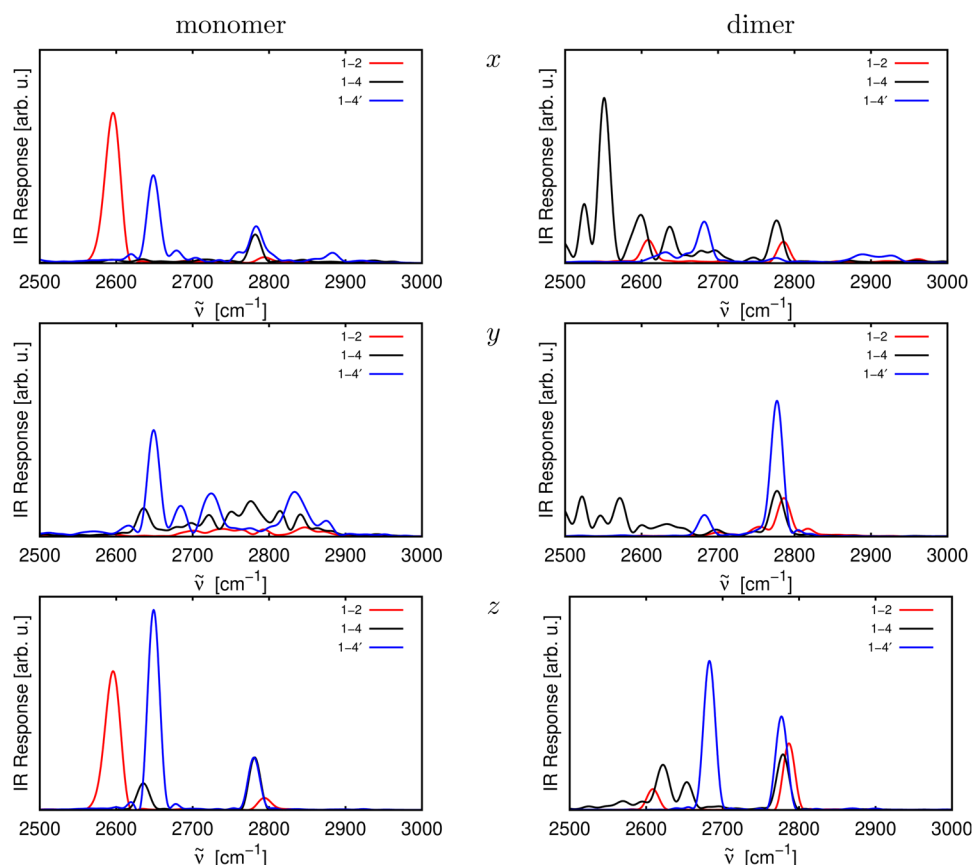


FIG. 3. IR spectra of dissociated D_2O on $\alpha\text{-Al}_2\text{O}_3(0001)$, obtained from the real part of the first-order susceptibility as $\text{Re}\{\chi_{aa}^{(1)}(\omega)\}$, with different polarization axes a , namely, x (upper panels), y (middle panels), and z (lower panels). In the left panels, the IR spectra for the “monomer” dissociated species (coverage 1/4) are shown, and in the right panels, the corresponding “dimer” dissociated species (coverage 1/2) are considered. The IR intensities are given in “arbitrary units,” with the full ranges for the monomers obeying the ratio 2:1:4 for $x:y:z$ and for dimers 1:2:2.

in the high-energy region around 2900 cm^{-1} we find resonances, attributable to the OD_{ads} fragments. In summary, for the dimer structures, we obtain IR spectra with similar basic features as for the monomeric cases, however, with rather different intensities. If we exclude the interesting behavior of 1-4, we relate the different intensities to local structural fluctuations, which for dimers are affected by the formation of temporary hydrogen bonds. We conclude that intensities are hence sensitive to the coverage, largely because of enhanced interactions between OD species.

D. VSF spectra from NVT/AIMD simulations

While direct validation of computed IR spectra with the experiment is not available so far, VSF spectra obtained from theory can be compared with experimental ones, which have been collected for D_2O on Al-terminated $\alpha\text{-Al}_2\text{O}_3(0001)$ in Ref. 24. The coverage was very low in these experiments but not unequivocally defined as in our structural models. In Ref. 24, both *ppp*- and *ssp*-polarization schemes (and two experimental geometries) had been employed. Here, we present theoretical VSF spectra for *ssp*, i.e., as $|\chi_{xxz}^{(2)}|^2$. The calculation of *ppp*-polarized VSF spectra would require a weighted averaging over several tensor elements, which we have not attempted here. We show *ssp*-polarized VSF signals in Fig. 4, for the monomer (left panel) and dimer (right panel) dissociated structures.

The spectra in the left panel show that the OD_{surf}^{1-2} VSF signal at the *xxz*-polarization, around 2600 cm^{-1} , is by far the most intense. In fact, the OD_{ads}^{1-2} peak at around 2800 cm^{-1} , which was slightly noticeable in the *z*-polarized IR spectrum of Fig. 3 and in the VDOS curves, is now not seen on the scale of Fig. 4—it is about of factor 2000 weaker than OD_{surf}^{1-2} . For the 1-4 and 1-4' structures, both peaks (for surface and adsorbate OD groups) are clearly seen in each case; however, their intensities are by far less intense than the OD_{ads}^{1-2} peak. Considering that under thermal equilibrium conditions at 300 K, the 1-4 and 1-4' adsorbates are minor species, one would expect that the dominance of OD_{ads}^{1-2} is even more severe. For 1-4', around 2570 cm^{-1} , a shoulder to the main peak at 2640 cm^{-1} is found, which could be assigned to a fluctuating hydrogen bonded vibration between the two OD fragments which is captured, thanks to the finite-temperature AIMD sampling. In Table III, we list peak positions, along with computed linewidths 2Γ (Full Width at Half Maximum) and intensities, relative to the most intense resonance. We note that intensities have to be taken with care since no weighting with the (unknown) population of each species (Boltzmann or non-Boltzmann) was made, i.e., strictly, only intensities for a given model (e.g., OD_{ads}^{1-2} with OD_{surf}^{1-2}) can be compared to each other.

In the experiment,²⁴ (with the aid of NMA from theory), at the *ssp*-polarization, resonances for $OD_{\text{surf}}^{1-4'}$, OD_{ads}^{1-4} and $OD_{\text{ads}}^{1-4'}$ (the

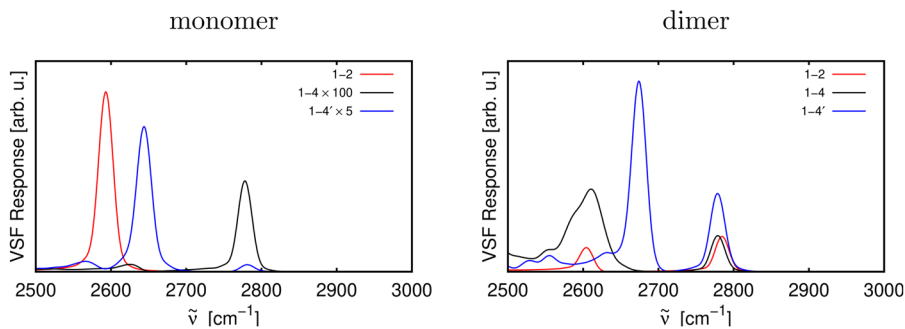


FIG. 4. VSF signals representative for *ssp*-polarized experiments, obtained as $I_{ssp}^{VSF} \propto |\chi_{xxz}^{(2)}(\omega)|^2$. The left panel shows the VSF spectra for the “monomeric” dissociated species, while in the right panel spectra are shown for the “dimeric” dissociated models. For the left panel, scaling factors have been used as shown for 1-4 and 1-4’ to make the figure clearer.

latter two merged in one peak), and OD_{ads}^{1-2} have been assigned, with the latter being the most intense and $OD_{surf}^{1-4'}$ being the least intense. With a different geometry and *ppp*-polarization, resonances for the “surface OD” species, OD_{surf}^{1-2} , OD_{surf}^{1-4} , and $OD_{surf}^{1-4'}$, were reported. Both spectra (*ssp* and *ppp*) differ substantially with respect to their peak intensities—in fact, only with two different polarizations, all resonances shown in Tables II and III are present. In Table III, the VSF experimental intensities relative to the most intense peak for a given polarization are reported, along with experimental linewidths 2Γ and, again, the experimental wavenumbers $\tilde{\nu}$ from Table II.

Referring to Table III, we first of all recall that comparison between theory and experiment is not expected to be quantitative because (i) the coverage in theoretical models is higher than realized in the experiment and (ii) *ppp*-polarization was not considered in theory as outlined. On top, in experiments, the surface was prepared at $T = 300$ K, but VSF measurements were carried out at lower T , whereas our simulations refer to 300 K throughout. Keeping these aspects in mind, we can still make the following observations: there is a certain mismatch of absolute frequencies, while frequency differences are reliable as outlined earlier. We find that theoretical and experimental linewidths agree very well for the “surface OD” species, while the spectral linewidths for the “adsorbate OD” are

larger compared to the experiment, by a factor of about two. We note, however, that in the experiment the signal-to-noise ratio is much worse for *ssp* than for *ppp*, and thus peak widths at the *ssp*-polarization are not clear. We made sure by test calculations that the theoretical linewidths are mostly due to dynamics and not due to the limited resolution of the Fourier transformation. As far as *ssp*-intensities are concerned, it is not so easy to bring theory and experiment together. Under *ssp*-polarization (the only one considered in our simulations), we note that according to theory $OD_{surf}^{1-4'}$ is less intense than $OD_{ads}^{1-4}/OD_{ads}^{1-4'}$, in agreement with the experiment. However, according to the experiment, OD_{ads}^{1-2} should be the most intense, contrary to what predicted with simulations. Of course, this may change when the fact is accounted for that 1-2 is the thermodynamically most stable species. On the other hand, from theory we should expect that OD_{surf}^{1-2} is seen also in an *ssp*-polarized VSF experiment (and not only for *ppp*), which is not the case according to Ref. 24. In fact, OD_{surf}^{1-2} should be by far the most intense peak of all. In summary, when comparing experimental with theoretical VSF spectra, we conclude that, in the “monomer” model (coverage 1/4), frequency spacings between resonances agree very well (absolute frequencies reasonably well after frequency scaling), linewidths are in partial agreement with experiment, while intensities seem to deviate from each other.

TABLE III. Characteristics of VSF spectra for dissociated D_2O at low coverage on an Al-terminated $\alpha-Al_2O_3(0001)$ surface. We show experimental peak positions $\tilde{\nu}$ again, along with corresponding VSF linewidths and relative intensities, the latter separately for *ssp*- and *ppp*-polarization. In the right half of the table, the corresponding information as obtained by theory is given, where $\tilde{\nu}_{max}$ now refers to the maximum of the VSF peaks. All frequencies/widths are given in cm^{-1} .

Assignment	Expt. ^a			Theory, monomer		
	$\tilde{\nu}$	I^{VSF} (pol.)	2Γ	$\tilde{\nu}_{max}$	I^{VSF} (pol.)	2Γ
OD_{surf}^{1-2}	2729 ± 5	0.39 (<i>ppp</i>)	24	2593	1.00 (<i>ssp</i>)	24
OD_{surf}^{1-4}	2764 ± 5	0.52 (<i>ppp</i>)	22	2630	0.002 (<i>ssp</i>)	18
$OD_{surf}^{1-4'}$	2790 ± 3	1.00 (<i>ppp</i>)	0.11 (<i>ssp</i>)	20	0.006 (<i>ssp</i>)	18
OD_{ads}^{1-4}	2900 ± 7		0.91 ^b (<i>ssp</i>)	40	0.144 (<i>ssp</i>)	13
$OD_{ads}^{1-4'}$	2900 ± 7		0.91 ^b (<i>ssp</i>)	40	0.005 (<i>ssp</i>)	15
OD_{ads}^{1-2}	2910 ± 7		1.00 (<i>ssp</i>)	42	0.0005 (<i>ssp</i>)	...

^aFrom Ref. 24.

^bBoth species seen as one peak with relative intensity 0.91.

Possible reasons for this mismatch in intensities are as follows. First of all, in the experiment, it is not entirely clear what “low coverage” means quantitatively. In particular, the surface coverage defined in theoretical models is most probably higher than in experiments, which obviously has a direct consequence on the VSF spectra. In fact, from Fig. 4, right panel, we see that by going to even higher coverage, namely, a coverage of 1/2, the VSF spectra depend sensitively on it, as already observed for IR spectra above. Again, we should stress that for such coverage only few of possible dimeric minima have been investigated so that a full structural sampling may lead to different vibrational responses. While peak positions and peak widths are not so much dependent on the presence of additional water fragments (apart from the fact that new peaks occur, as for IR), the signal intensities are very strongly affected. In fact, from the right panel of Fig. 4, we note that now, for the 1-2 species, for example, the *ssp* signal of $\text{OD}_{\text{ads}}^{1-2}$ is more intense than the $\text{OD}_{\text{surf}}^{1-2}$ peak, which is qualitatively in line with the experiment. Also, the 1-2 resonances are no longer dominant over the 1-4 and 1-4' signals, at least when not considering that the latter are minor species. This could explain why these less stable species are seen in the experiment.

Surface coverage accompanied by local interactions among “adsorbate OD” and “surface OD” also affects their average orientations. As described in Appendix B, the orientation assumed by OD_{surf} bonds, which is reflected by their angular distributions, is extremely sensitive to the vicinity of the neighboring OD_{ads} . Moreover, because of finite-temperature AIMD propagation, the angular distributions can span over several degrees. Thermally induced fluctuations in OD orientations are definitely more marked in our AIMD than in the common experimental assumption/condition,^{24,68} where the orientational motion is considered very slow, potentially influencing the spectroscopic signals. This assumption has also been the subject of recent works,^{69,70} which have underlined the relationship between VSF response and the time scale in which an oscillator reorients.

We should also mention that an *ssp*-polarized VSF spectrum is not exactly equal to $|\chi_{xxz}^{(2)}(\omega)|^2$, and also corresponding Fresnel factors for the given polarization scheme should be considered. We tested corrections by Fresnel factors^{24,71} for our systems but did not find any significant changes in the calculated VSF spectral responses. Finally, being limited to tens of picoseconds, our model does not allow for the formation of surface defects and/or the full equilibration between different adsorbate species. Certainly, also the experiments leave room for improvement since the signals are weak and line fitting comes with considerable errors.

V. SUMMARY AND CONCLUSIONS

In this work, we applied an efficient computational protocol⁴² based on velocity-velocity autocorrelation functions, sampled from canonical *ab initio* molecular dynamics trajectories at 300 K, to obtain vibrational spectra (VDOS, IR, and VSF) of dissociatively adsorbed D_2O structures on the Al-terminated $\alpha\text{-Al}_2\text{O}_3(0001)$ surface. The AIMD was based on periodic DFT at the PBE+D2 level of theory, the same method which previously had been applied in the context of static calculations including normal mode analysis. The AIMD/correlation function protocol had also successfully been applied to the hydroxylated form of $\alpha\text{-Al}_2\text{O}_3(0001)$,¹⁸ showing that it is capable of providing spectroscopic signatures beyond static

calculations and NMA for alumina in contact with (nondissociated) water. It was one of the methodological aims of this work to go beyond the static NMA approach to dissect vibrational peaks associated with OD fragments resulting from water dissociation on the Al-terminated surface.

The approach has been applied, using a 1/4 coverage model [one D_2O molecule per (2×2) cell], to three dissociated D_2O structures, 1-2, 1-4, and 1-4'. These had been suggested as particularly stable dissociation products of water at low coverage on the mentioned surface.^{11,14,23,24} To allow for higher coverage, also closely related, 1/2 coverage models [two D_2O molecules per (2×2) cell] were studied.

Focusing primarily on the singly dissociated forms, we examined how static vibrational frequencies at the PBE+D2 level of theory provide a good agreement with experimental findings, as far as frequency spacings between various “OD surface” and “OD adsorbate” species are concerned. Quantitatively, however, there is a constant ($\sim 100 \text{ cm}^{-1}$) red-shift of harmonic PBE+D2 frequencies in agreement with Refs. 21 and 24. Employing appropriate scaling factors for vibrational frequencies⁶⁷ improves the agreement considerably, bringing theoretical frequencies up to 20–35 cm^{-1} close to the experiment. Introducing dynamical effects and anharmonicity through AIMD at 300 K, on the other hand, the vibrational frequencies are (further) red-shifted by $\sim 10\text{--}40 \text{ cm}^{-1}$, making the agreement between experiment and theory worse again. We also find that the anharmonic corrections are considerably smaller in classical AIMD compared to a quantum mechanical treatment because only low-energy parts of the potential energy surface are probed in classical mechanics. In Ref. 21, it has been shown that the use of higher level electronic structure method can lead to vibrational frequencies in better agreement with experimental values already without scaling and in even better agreement with scaling. Still, all theoretical frequencies appear to be red-shifted with respect to suggested experimental values, when the ideal surface models used here are adopted. In particular, no very high frequencies close to 2900 cm^{-1} suggested by the experiment²⁴ have been found in theory by NMA and simple anharmonic corrections to it. Interestingly, such high frequencies do show up already in unscaled AIMD, when looking at spectroscopic signals, e.g., *x* and *y*-polarized IR spectra (cf. Fig. 3). We cannot claim here with certainty that the unusual, high-frequency peaks proposed in Ref. 24 are fully confirmed by theory; however, our work shows that dynamics, in particular, when probing regions of the potential surface outside the directions of normal modes, can lead to unusual peak positions. In concert with the findings made in Ref. 21 that the frequencies are considerably higher when hybrid functionals are used instead of Generalized Gradient Approximation (GGA) functionals as here, it seems fair to say that the occurrence of high-frequency signals (around 2900 cm^{-1}) in vibrational spectra of $\text{D}_2\text{O}/\alpha\text{-Al}_2\text{O}_3(0001)$ is not unrealistic.

Another effect of thermal motion is line broadening. Comparing experimental linewidths for VSF signals as suggested in Ref. 24 to the theoretical linewidths computed here by AIMD shows that at least for the “OD surface” species good agreement ($2\Gamma \sim 20 \text{ cm}^{-1}$). The linewidths of the “OD adsorbate” species seem to be underestimated somewhat, by a factor of about two. The reasons are unknown so far; however, we note again that classical AIMD probes the bottom of a potential well only, where vibrations are of low amplitude. In general, contributions by quantum mechanical

treatment of nuclei to the broadening are absent. Therefore, a narrower distribution can be expected in AIMD.

While theoretical peak positions and linewidths are in reasonably good agreement with experimental observations, only poor agreement concerning line intensities in VSF spectra was found. For example, the relatively high intensity of VSF signals of 1-4 and 1-4' in the experiment is surprising, given that the latter are minor species at least under thermal equilibrium conditions and given the fact that our calculations suggest intense peaks, in particular, for $\text{OD}_{\text{surf}}^{1-2}$.

Using simple periodic models with higher coverage (1/2), we have seen, however, that VSF intensities depend very sensitively on coverage. This suggests that the ideal, perfect 1/4 coverage surface models may not be fully realistic. Rather, the presence of defects (experimentally in the process of surface preparation and/or in theory in the course of long-time thermalization), local water clustering, and, generally, the trapping of nonequilibrium configurations over long time periods after molecular beam dosing may have a pronounced effect on measured spectra. In summary, the vibrational spectroscopy of water-covered alumina surfaces continues to be a challenging, interesting subject.

ACKNOWLEDGMENTS

The authors thank the Deutsche Forschungsgemeinschaft (DFG) for support of this work through Collaborative Research Center 1109, *Understanding of Metal Oxide/Water Systems at the Molecular Scale*, and the North-German Supercomputing Alliance (HLRN) for providing HPC resources that have contributed to the research results reported in this paper. G.M. thanks the International Max Planck Research School (IMPRS) on *Functional Interfaces in Physics and Chemistry* for support.

APPENDIX A: PROTON TRANSFER IN THE 1-4 DIMER

As mentioned in the main text, during the canonical AIMD simulations for the 1-4 dimeric structure, we observed a proton (more precisely, deuteron) transfer reaction from one of the two OD_{surf} terminations to form a molecularly adsorbed D_2O , leading to a mixed dissociated and molecular configuration. In one of the

two trajectories where such an event occurred, the D atom “jumped” relatively fast and moved to form D_2O after 400 fs. In the other reactive trajectory, such transfer happened later, after nearly 3 ps. In both of the two trajectories, no backreaction was observed, suggesting that the new mixed structure is energetically stabilized.

In order to rationalize these findings from a different angle, we performed nudged elastic band calculations⁶⁵ at the DFT/PBE+D2 level of theory as implemented by the VTST package for VASP. Here, we report the results obtained with the Climbing Image Nudged Elastic Band (CI-NEB) method⁶⁶ to study the reaction from the 1-4 doubly dissociated dimer to the new (optimized) mixed structure. The result is shown in Fig. 5.

As we see from the figure, the deuterium transfer leads to an energetically favored mixed product, which is about 0.42 eV more stable than the educt configuration. Looking in more detail at the total energy profile (red curve), a possible transition state was found at the second CI-NEB image, with an activation energy $\Delta E^\ddagger = E^\ddagger - E(\text{educt})$ being only 0.01 eV (\ddagger indicates a transition state). Static NMA calculations on this structure retrieved a single imaginary frequency, indicating a transition state. We also calculated an activation free energy, $\Delta G^\ddagger = G^\ddagger - G(\text{educt})$ at 300 K, giving 0.036 eV. We may also estimate a rate for the reaction, using Eyring's equation $k(T) = \frac{k_B T}{h} e^{-\Delta G^\ddagger(T)/k_B T}$, giving $k = 1.53 \times 10^{12} \text{ s}^{-1}$. We thus expect a transfer process on the time scale of picoseconds, which makes our observations in AIMD plausible. A backreaction will happen on much longer time scales since then the activation free energy is an order of magnitude larger. We note that PBE+D2 usually underestimates activation barriers and overestimates rates (see Ref. 21 for a quantitative statement), but it is nevertheless conceivable that ultrafast proton (deuteron) transfers will happen on the water/alumina interface.

A pending question concerns why such a phenomenon has been observed only for the 1-4 dimeric structure and not for the other two dimers as well, at least within the limited simulation times adopted here. A possible explanation is the fact that the 1-4 dissociated dimer structure is the least stable according to Table 1 (in contrast to the monomer, where 1-4' is the least stable). Furthermore, among the possible dissociation sites (1-2, 1-4, and 1-4'), the 1-4 configuration allows for an intermediate distance between

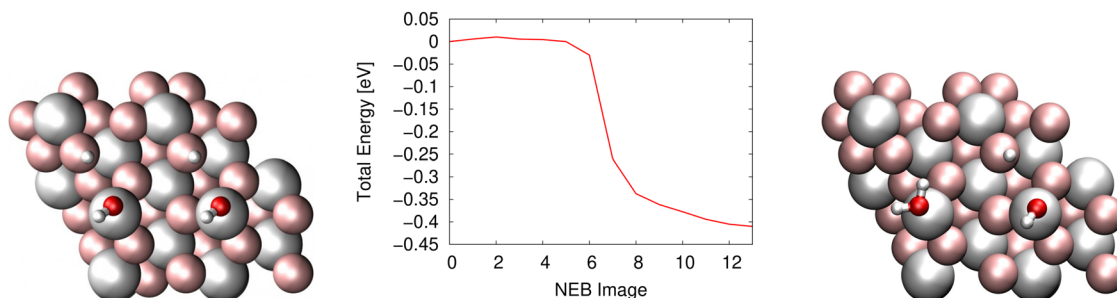


FIG. 5. Reaction profile for the proton (deuteron) transfer in the 1-4 dimer model. In the doubly dissociated model (left), a deuteron moves from an OD_{surf} fragment to an OD_{ads} fragment to form molecularly adsorbed D_2O , in a mixed configuration (right). In the middle, a CI-NEB path is shown, showing that the mixed configuration is more stable and separated from the reactant configuration by a very shallow barrier only.

the “OD surface” and “OD adsorption” fragments (around 2.85 Å), which may be favorable for deuteron motion: In 1-2, this distance may be too short (~ 2.5 Å) and lead to a greater steric hindrance in the 1-2 structure or too large for 1-4' (~ 4.1 Å) for an effective deuteron transfer to take place.

APPENDIX B: ORIENTATIONAL DISTRIBUTION OF OD BONDS

In the main text, we have shown that even at low coverages (1/4 and 1/2) structural fluctuations affect vibrational (IR and VSF)

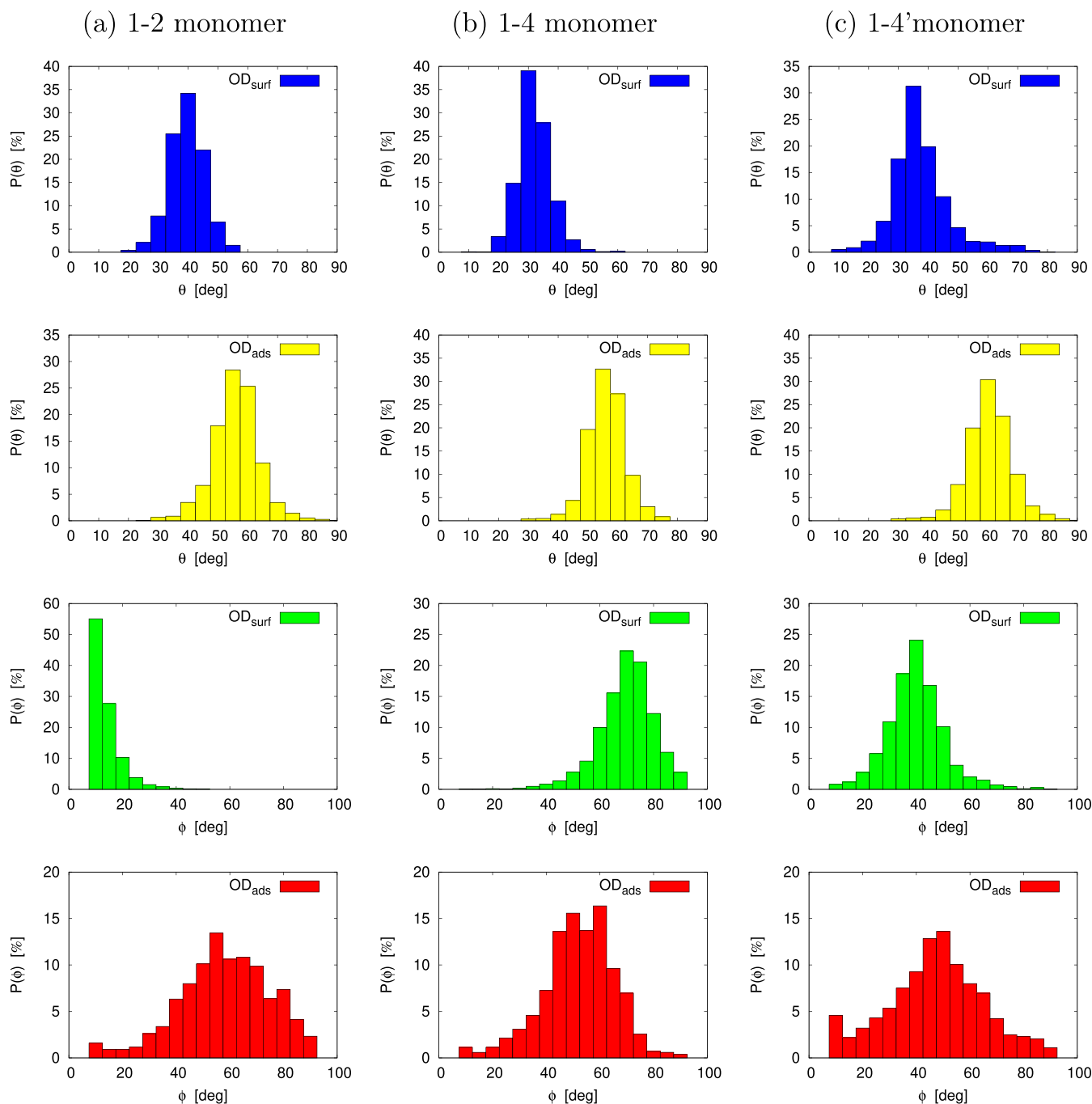


FIG. 6. Ensemble-averaged, percentage probability distributions of polar and azimuthal angles, $P(\theta)$ and $P(\phi)$, for both OD_{surf} and OD_{ads} fragments during AIMD trajectories at 300 K. Each column corresponds to the different monomer dissociated structures: (a) 1-2, (b) 1-4, and (c) 1-4'.

spectra. In this Appendix, we want to further analyze orientational behavior of the various OD bonds during NVT/AIMD trajectories at 300 K. To this end, in Figs. 6 and 7, we show angular distributions for both OD_{surf} and OD_{ads} fragments for all monomeric

and dimeric, dissociated starting structures. In particular, we calculated angular distribution (percentage) probabilities as $P(\theta) = \frac{n_\theta}{N_t} \times 100\%$ and $P(\phi) = \frac{n_\phi}{N_t} \times 100\%$. Here, n_θ and n_ϕ are the numbers of time steps associated with a certain value of the polar (θ)

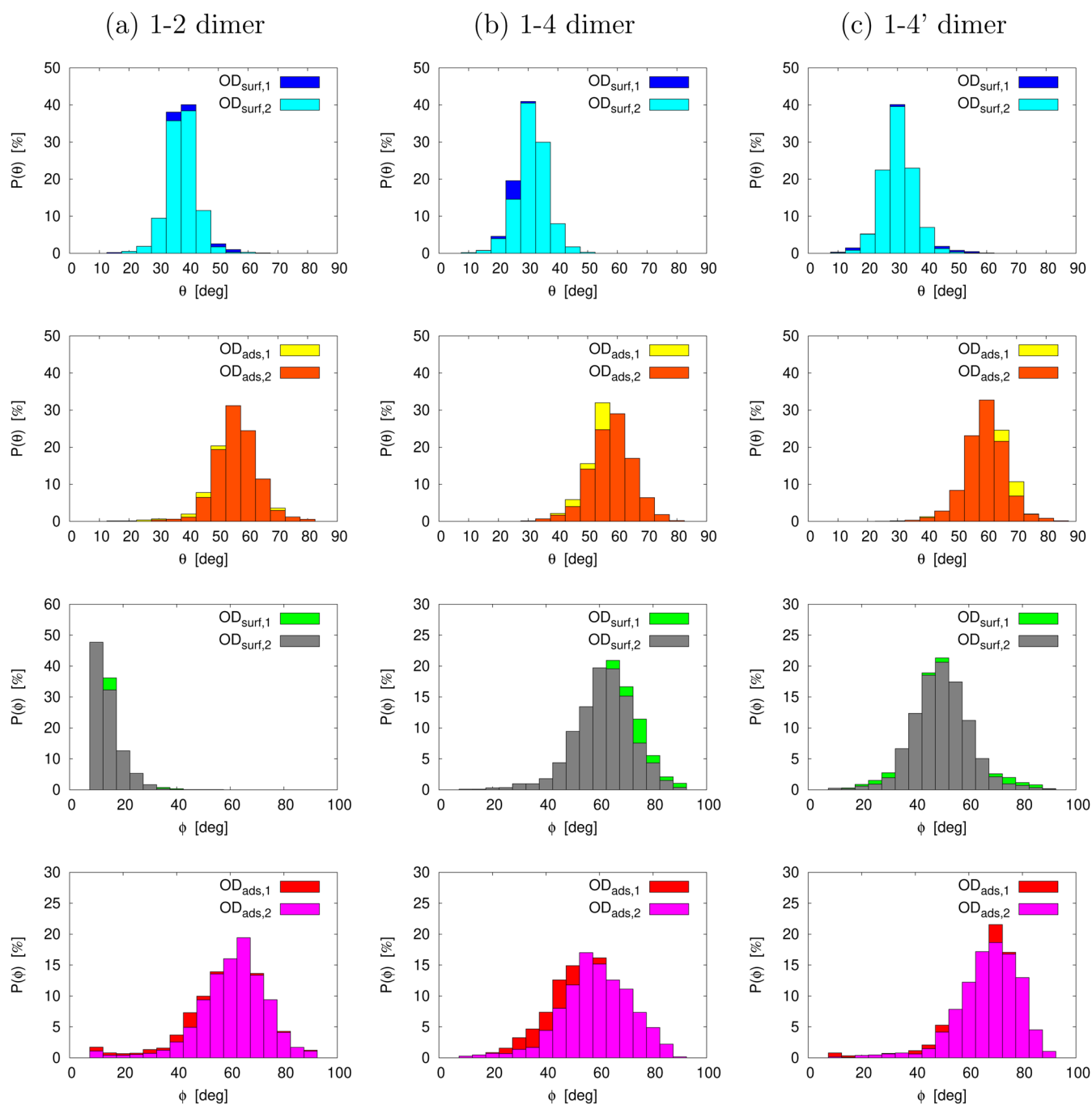


FIG. 7. Ensemble-averaged, percentage probability distributions of polar and azimuthal angles, $P(\theta)$ and $P(\phi)$, for all four OD_{surf} and OD_{ads} fragments during AIMD trajectories at 300 K. Each column corresponds to the different dimer dissociated structures: (a) 1-2, (b) 1-4, and (c) 1-4'.

and the azimuthal (ϕ) angles in “boxes” 5° wide (see figure), and N_t is the total number of time steps. The polar and azimuthal angles are, respectively, defined as $\theta = \arccos(\frac{z_{OD}}{l_{OD}})$ and $\phi = \arctan(\frac{y_{OD}}{x_{OD}})$, where q_{OD} ($q = x, y, z$) indicates the q th Cartesian component of an OD interatomic bond vector (see Fig. 1 for the coordinate system), and l_{OD} is the bond length corresponding to this bond vector.

Looking at the monomer dissociated samples first, from Fig. 6 we note that the three 1-2, 1-4, and 1-4' structures are characterized by an increasing conformational freedom, thanks to the larger distance between dissociated D_2O fragments. We can observe that while OD polar angles seem not to be greatly affected by how close OD_{surf} and OD_{ads} are, the lower panels of Fig. 6 clearly show that the “in-plane” angular dynamics depends on steric hindrance especially for the OD_{surf} fragment.

Similar arguments can be put forward for the dissociated, bimolecular structures reported in Fig. 7. Looking at both polar and azimuthal angular distributions, we retrieve similar features as observed above. While the relative symmetry of adsorption sites seems to generally characterize the orientational dynamics of dimeric structures, we notice that in the 1-4 dimer case the two OD_{surf} bonds have on average a slightly “uneven” behavior. This special feature can again be explained with the occurrence of trajectories affected by D atom transfer.

REFERENCES

- 1 P. A. Cox and V. E. Henrich, *The Surface Science of Metal Oxides* (Cambridge University Press, Cambridge, 1994).
- 2 H.-J. Freund, H. Kühlenbeck, and V. Staemmler, *Rep. Prog. Phys.* **59**(3), 283 (1996).
- 3 G. E. Brown, V. E. Henrich, W. H. Casey, D. L. Clark, C. Eggleston, A. Felmy, D. W. Goodman, M. Grätzel, G. Maciel, M. I. McCarthy, K. H. Nealsen, D. A. Sverjensky, M. F. Toney, and J. M. Zachara, *Chem. Rev.* **99**(1), 77–174 (1999).
- 4 M. A. Henderson, *Surf. Sci. Rep.* **46**, 1–308 (2002).
- 5 O. Bjørneholm, M. H. Hansen, A. Hodgson, L.-M. Liu, D. T. Limmer, A. Michaelides, P. Pedevilla, J. Rossmeisl, H. Shen, G. Tocci, E. Tyrode, M.-M. Walz, J. Werner, and H. Bluhm, *Chem. Rev.* **116**(13), 7698–7726 (2016).
- 6 Y. Wang and C. Wöll, *Chem. Soc. Rev.* **46**(7), 1875–1932 (2017).
- 7 R. Mu, Z. Zhao, Z. Dohnalek, and J. Gong, *Chem. Soc. Rev.* **46**(7), 1785–1806 (2017).
- 8 M. E. McBriarty, G. F. von Rudorff, J. E. Stubbs, P. J. Eng, J. Blumberger, and K. M. Rosso, *J. Am. Chem. Soc.* **139**(7), 2581–2584 (2017).
- 9 Z.-J. Zhao, Z. Li, Y. Cui, H. Zhu, W. F. Schneider, W. N. Delgass, F. Ribeiro, and J. Greeley, *J. Catal.* **345**, 157–169 (2017).
- 10 M.-P. Gaigeot, M. Sprik, and M. Sulpizi, *J. Phys.: Condens. Matter* **24**(12), 124106 (2012).
- 11 K. C. Hass, W. F. Schneider, A. Curioni, and W. Andreoni, *Science* **282**(5387), 265–268 (1998).
- 12 P. Liu, T. Kendelewicz, G. E. Brown, Jr., E. J. Nelson, and S. A. Chambers, *Surf. Sci.* **417**(1), 53–65 (1998).
- 13 P. J. Eng, T. P. Trainor, G. E. Brown, Jr., G. A. Waychunas, M. Neville, S. R. Sutton, and M. L. Rivers, *Science* **288**(5468), 1029–1033 (2000).
- 14 K. C. Hass, W. F. Schneider, A. Curioni, and W. Andreoni, *J. Phys. Chem. B* **104**(23), 5527–5540 (2000).
- 15 L. Zhang, C. Tian, G. A. Waychunas, and Y. R. Shen, *J. Am. Chem. Soc.* **130**(24), 7686–7694 (2008).
- 16 J. G. Catalano, *Geochim. Cosmochim. Acta* **75**(8), 2062–2071 (2011).
- 17 S. Heiden, J. Wirth, R. K. Campen, and P. Saalfrank, *J. Phys. Chem. C* **122**(27), 15494–15504 (2018).
- 18 G. Melani, Y. Nagata, J. Wirth, and P. Saalfrank, *J. Chem. Phys.* **149**(1), 014707 (2018).
- 19 N. G. Petrik, P. L. Huestis, J. A. LaVerne, A. B. Aleksandrov, T. M. Orlando, and G. A. Kimmel, *J. Phys. Chem. C* **122**(17), 9540–9551 (2018).
- 20 M. DelloStritto, S. M. Piontek, M. L. Klein, and E. Borguet, *J. Phys. Chem. C* **122**(37), 21284–21294 (2018).
- 21 S. Heiden, D. Usvyat, and P. Saalfrank, *J. Phys. Chem. C* **123**(11), 6675–6684 (2019).
- 22 T. Kurita, K. Uchida, and A. Oshiyama, *Phys. Rev. B* **82**(15), 155319 (2010).
- 23 J. Wirth and P. Saalfrank, *J. Phys. Chem. C* **116**(51), 26829–26840 (2012).
- 24 H. Kirsch, J. Wirth, Y. Tong, M. Wolf, P. Saalfrank, and R. K. Campen, *J. Phys. Chem. C* **118**(25), 13623–13630 (2014).
- 25 Y. Tong, J. Wirth, H. Kirsch, M. Wolf, P. Saalfrank, and R. K. Campen, *J. Chem. Phys.* **142**(5), 054704 (2015).
- 26 J. Wirth, H. Kirsch, S. Wlosczyk, Y. Tong, P. Saalfrank, and R. K. Campen, *Phys. Chem. Chem. Phys.* **18**, 14822 (2016).
- 27 S. Heiden, Y. Yue, H. Kirsch, J. Wirth, P. Saalfrank, and R. K. Campen, *J. Phys. Chem. C* **122**(12), 6573–6584 (2018).
- 28 X. D. Zhu, H. Suhr, and Y. R. Shen, *Phys. Rev. B* **35**, 3047–3050 (1987).
- 29 J. F. D. Liljeblad and E. Tyrode, *J. Phys. Chem. C* **116**(43), 22893–22903 (2012).
- 30 H.-F. Wang, L. Velarde, W. Gan, and L. Fu, *Annu. Rev. Phys. Chem.* **66**, 189–216 (2015).
- 31 P. A. Covert and D. K. Hore, *Annu. Rev. Phys. Chem.* **67**(1), 233–257 (2016).
- 32 L. Dalstein, E. Potapova, and E. Tyrode, *Phys. Chem. Chem. Phys.* **19**, 10343–10349 (2017).
- 33 M. R. Fagiani, X. Song, S. Debnath, S. Gewinner, W. Schöllkopf, K. R. Asmis, F. A. Bischoff, F. Müller, and J. Sauer, *J. Phys. Chem. Lett.* **8**(6), 1272–1277 (2017).
- 34 M. DelloStritto and J. Sofo, *J. Phys. Chem. A* **121**(16), 3045–3055 (2017).
- 35 D. A. McQuarrie, *Statistical Mechanics* (University Science Books, 2000).
- 36 B. J. Berne and G. D. Harp, *Adv. Chem. Phys.* **17**, 63–227 (1970).
- 37 A. Perry, C. Neipert, B. Space, and P. B. Moore, *Chem. Rev.* **106**(4), 1234–1258 (2006).
- 38 Y. Nagata and S. Mukamel, *J. Am. Chem. Soc.* **132**(18), 6434–6442 (2010).
- 39 J. L. Skinner, P. A. Pieniazek, and S. M. Gruenbaum, *Acc. Chem. Res.* **45**(1), 93–100 (2012).
- 40 M. Sulpizi, M. Salanne, M. Sprik, and M.-P. Gaigeot, *J. Phys. Chem. Lett.* **4**(1), 83–87 (2013).
- 41 P. Huang, T. A. Pham, G. Galli, and E. Schwegler, *J. Phys. Chem. C* **118**(17), 8944–8951 (2014).
- 42 T. Ohto, K. Usui, T. Hasegawa, M. Bonn, and Y. Nagata, *J. Chem. Phys.* **143**(12), 124702 (2015).
- 43 S. Luber, *J. Phys. Chem. Lett.* **7**, 5183–5187 (2016).
- 44 M.-P. Gaigeot and M. Sulpizi, *Mineral/Water Interaction* (John Wiley & Sons, 2016), pp. 271–309.
- 45 A. Morita and J. T. Hynes, *Chem. Phys.* **258**(2), 371–390 (2000).
- 46 A. Morita and J. T. Hynes, *J. Phys. Chem. B* **106**(3), 673–685 (2002).
- 47 T. Ishiyama and A. Morita, *J. Phys. Chem. C* **111**(2), 721–737 (2007).
- 48 T. Ishiyama, T. Imamura, and A. Morita, *Chem. Rev.* **114**(17), 8447–8470 (2014).
- 49 T. Ishiyama and A. Morita, *Annu. Rev. Phys. Chem.* **68**(1), 355–377 (2017).
- 50 R. W. Nunes and X. Gonze, *Phys. Rev. B* **63**, 155107 (2001).
- 51 A. A. Mostofi, J. R. Yates, G. Pizzi, Y.-S. Lee, I. Souza, D. Vanderbilt, and N. Marzari, *Comput. Phys. Commun.* **185**, 2309–2310 (2014).
- 52 R. Khatib and M. Sulpizi, *J. Phys. Chem. Lett.* **8**(6), 1310–1314 (2017).
- 53 S. Housseinpour, F. Tang, F. Wang, R. A. Livingstone, S. J. Schlegel, T. Ohto, M. Bonn, Y. Nagata, and E. H. G. Backus, *J. Phys. Chem. Lett.* **8**, 2195–2199 (2017).
- 54 S. A. Corcelli and J. L. Skinner, *J. Phys. Chem. A* **109**(28), 6154–6165 (2005).
- 55 B. M. Auer and J. L. Skinner, *J. Chem. Phys.* **128**(22), 224511 (2008).
- 56 T. Ohto, H. Tada, and Y. Nagata, *Phys. Chem. Chem. Phys.* **20**, 12979–12985 (2018).
- 57 W. Kohn and L. J. Sham, *Phys. Rev.* **140**, 1133–1138 (1965).

- ⁵⁸J. P. Perdew, K. Burke, and M. Ernzerhof, *Phys. Rev. Lett.* **77**(18), 3865–3868 (1996).
- ⁵⁹P. E. Blöchl, *Phys. Rev. B* **50**(24), 17953–17979 (1994).
- ⁶⁰G. Kresse and J. Hafner, *Phys. Rev. B* **47**(1), 558–561 (1993).
- ⁶¹G. Kresse and J. Hafner, *Phys. Rev. B* **48**(17), 13115–13118 (1993).
- ⁶²G. Kresse and D. Joubert, *Phys. Rev. B* **59**(3), 1758–1775 (1999).
- ⁶³S. Grimme, *J. Comput. Chem.* **27**(15), 1787–1799 (2006).
- ⁶⁴S. Nosé, *Mol. Phys.* **52**(2), 255–268 (1984).
- ⁶⁵H. Jónsson, M. Greg, and K. W. Jacobsen, *Nudged Elastic Band Method for Finding Minimum Energy Paths of Transitions* (World Scientific, 1995), pp. 385–404.
- ⁶⁶G. Henkelman, B. P. Uberuaga, and H. Jónsson, *J. Chem. Phys.* **113**(22), 9901–9904 (2000).
- ⁶⁷M. K. Kesharwani, B. Brauer, and J. M. L. Martin, *J. Phys. Chem. A* **119**(9), 1701–1714 (2015).
- ⁶⁸X. Wei and Y. R. Shen, *Phys. Rev. Lett.* **86**, 4799–4802 (2001).
- ⁶⁹S. Sun, F. Tang, S. Imoto, D. R. Moberg, T. Ohto, F. Paesani, M. Bonn, E. H. G. Backus, and Y. Nagata, *Phys. Rev. Lett.* **121**, 246101 (2018).
- ⁷⁰T. Ohto, M. Dodia, S. Imoto, and Y. Nagata, *J. Chem. Theory Comput.* **15**(1), 595–602 (2019).
- ⁷¹X. Zhuang, P. B. Miranda, D. Kim, and Y. R. Shen, *Phys. Rev. B* **59**, 12632–12640 (1999).